Maximum-Force-per-Ampere Strategy of Current Distribution for Efficiency Improvement in Planar Switched Reluctance Motors

Su-Dan Huang, Guang-Zhong Cao, *Member, IEEE*, Zheng-You He, *Senior Member, IEEE*, Chao Wu, Ji-An Duan, Norbert C. Cheung, *Senior Member, IEEE*, and Qing-Quan Qian

***Abstract*—This paper proposes a novel maximum-force-per-ampere strategy for the current distribution of planar switched reluctance motors (PSRMs) for efficiency improvement. This strategy is the first of its kind for planar motors, and it is used to generate the desired thrust force with the minimum sum of squares of the three-phase current. To formulate this strategy, a constrained optimization problem with time-varying parameters is first developed. Then, the problem is transformed into an unconstrained problem with a barrier function. Additionally, a self-designed adaptive genetic algorithm is introduced to solve the unconstrained optimization problem for locating the optimal currents. Comparative studies of the proposed and conventional strategies for a PSRM system are carried out via simulation and experiment, and planar trajectory tracking for the system with the proposed strategy is experimentally performed. The validity of the proposed strategy is also verified.**

***Index Terms*—Adaptive genetic algorithm (AGA), efficiency improvement, maximum-force-per-ampere (MFPA), planar switched reluctance motor (PSRM).**

I. Introduction

PRECISION positioning has played an ever increasing role to meet growing requirements of semiconductor lithography, scanning microscope, surface profilometer, etc. [1]–[4]. Compared to actuators achieving planar motion with complicated mechanical transmissions, planar motors are particularly attractive due to their advantages of direct drive, simple structure, high reliability, low friction, and no backlash [4]–[7]. Among different types of planar motors, the planar switched reluctance motor (PSRM) is a promising candidate since it features high precision, low cost, low heat loss, easy manufacture, and strong resilience to harsh environment [8]. However, the switched reluctance motor (SRM) is generally considered as a low-efficiency motor compared with the permanent-magnet motor [9].

Industrial applications demand high-efficiency electrical machines, and a wide variety of research works are aimed at improving their machine's efficiency [10]–[14]. For the emerging planar motors, efficiency improvement is a key factor to promote their adaptation to the industry. The main methods of improving the efficiency of planar motors are structural design improvement and advanced control strategies. For the structural design aspect, a new permanent-magnet array has been presented to improve efficiency for permanent-magnet planar motors in [15]; novel overlapping ironless windings for permanent-magnet planar motors have been designed, resulting in a larger force with the same copper losses in [16]. For the advanced control strategy aspect, an ohmic-loss reduction control strategy of planar motors has been proposed, but no experimental study has been given in [17]; a commutation strategy has been applied to magnetically levitated planar actuators, which minimizes the ohmic losses of coils through the 2-norm minimization of the current vector [18], [19]. However, no refereed literature has been reported on the efficiency improvement of the PSRM based on a specific control strategy. This paper aims to further fill this void by reporting on a theoretical and experimental study of efficiency improvement for the PSRM, which employs a novel current distribution method with a maximum-force-per-ampere (MFPA) strategy.

The MFPA strategy is first developed to fulfill the requirement of energy saving for planar motors. Under constant turn-on and turn-off positions of phase currents, this strategy is used to generate the desired instantaneous thrust force, with the minimum sum of squares of the three-phase current. This strategy is applicable to general operations of the PSRM. In such strategy, the efficiency of the PSRM is increased as the copper losses are minimized. As a current-minimizing technique, the MFPA requires a solution to find the optimal currents. The solution of the MFPA is very different from that of the

Manuscript received February 17, 2015; revised May 6, 2015 and July 28, 2015; accepted August 21, 2015. Date of publication October 19, 2015; date of current version February 8, 2016. This work was supported in part by the National Natural Science Foundation of China under Grant NSFC51275312 and Grant NSFC51207093, in part by the National Key Technology R&D Program under Grant 2014BAH23F04, and in part by the Shenzhen Government Fund under Grant KC2014JSJS025A, Grant JSGG20141015153303491, and Grant JCYJ20140418091413556.

S.-D. Huang is with the Shenzhen Key Laboratory of Electromagnetic Control, Shenzhen University, Shenzhen 518060, China, and also with the Department of Electrical Engineering, Southwest Jiaotong University, Chengdu 610031, China (e-mail: hsdsudan@gmail.com).

G.-Z. Cao and C. Wu are with the Shenzhen Key Laboratory of Electromagnetic Control, Shenzhen University, Shenzhen 518060, China (e-mail: gzcao.01@gmail.com; chaobb0791@hotmail.com).

Z.-Y. He and Q.-Q. Qian are with the Department of Electrical Engineering, Southwest Jiaotong University, Chengdu 610031, China (e-mail: hezy@swjtu.edu.cn; qqq@swjtu.edu.cn).

J.-A. Duan is with the State Key Laboratory of High-Performance Complex Manufacturing, Central South University, Changsha 410083, China (e-mail: duanjian@mail.csu.edu.cn).

N. C. Cheung is with the Department of Electrical Engineering, Hong Kong Polytechnic University, Kowloon, Hong Kong (e-mail: norbert.cheung@polyu.edu.hk).

Color versions of one or more of the figures in this paper are available online at http://ieeexplore.ieee.org.

Digital Object Identifier 10.1109/TIE.2015.2492948

maximum-torque-per-ampere (MTPA) widely applied to permanent-magnet synchronous motors [20]–[23] since the switched reluctance principle of the PSRM is distinctly different from the alternating current (ac) motor operating principle. The MTPA has been developed for the rotary SRM in recent years. There are two primarily applications. For the first application, the MTPA is applied to the vector control drive, based on the vector control of the ac motor. The aim is to minimize the magnitude of the current vector for generating desired instantaneous torque under constant root mean square (rms) current [24]. In the second application, to maximize the average torque with the same rms current or maximize the average torque per ampere, the MTPA is employed to optimize the turn-on and turn-off angular positions of phase currents [25], [26]. Since the physical and mathematical descriptions of the MTPA for the rotary SRM are different from those of the MFPA for the PSRM, the solution of the MTPA for the rotary SRM cannot be directly applied in the MFPA.

In this paper, the MFPA is formulated as a nonlinear constrained optimization problem, and its state continuously changes due to its time-varying parameters. The commonly used mathematical optimization methods, such as the quasi-Newton method and the method of Lagrange multipliers, are not appropriate for the MFPA because they cannot find the global optimal solution or cannot yield the optimality condition, particularly when the conditions are changing all the time. Hence, the MFPA is faced with a task of determining an effective optimization method featuring wide applicability and global optimization. Under this situation, the adaptive genetic algorithm (AGA) is found to be suitable for the optimization problem of the MFPA since its applicability and global optimization observably outperform other optimization methods, and the AGA exhibits features of easy implementation, strong robustness, and fast convergence [27]–[31]. Additionally, the constrained optimization problem solved by the AGA needs to be transformed into an unconstrained problem since the AGA is an unconstrained search procedure within a given search space [27]. However, the constraints can be handled via the barrier function.

This paper is concerned with the MFPA strategy of the current distribution of a PSRM for efficiency improvement using the AGA. The main contributions of this paper consist of the following: 1) developing a novel MFPA strategy for the PSRM to improve its efficiency; 2) extending the energy-saving study to the PSRM; and 3) demonstrating a systematic research of efficiency optimization for the PSRM using the proposed control strategy.

II. System Formulation of the PSRM

A. Mechanical Structure

The PSRM can be seen as two linear switched reluctance motors (LSRMs) with orthogonal magnetic circuits. The prototype of the PSRM developed in our laboratory is presented in Fig. 1, and its specifications are listed in Table I. The PSRM consists of a stator base, stator sets, x- and y-axes moving platforms, x- and y-axes linear encoders, and x- and y-axes linear guides. The y-axis moving platform consists of an x-axis moving platform and a sliding plate. The x-axis moving platform is composed of two sets of three identical movers. The two sets of movers are perpendicular to each other, and each set of movers is responsible for motion in its axis. Phases xa, xb, and xc and phases ya, yb, and yc are the three-phase winding in x- and y-axes, respectively. The stator block and mover are composed of a set of laminated silicon steels.

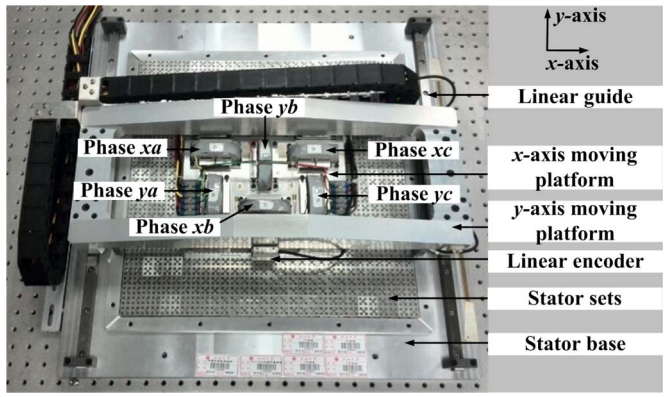

Fig. 1. Prototype of the PSRM.

TABLE I
Specifications of the PSRM

Parameters	Value
Tooth width of movers and stators	3.6 mm
Pole pitch of movers and stators	7.2 mm
Mass of x-axis moving platform	5.9 kg
Mass of y-axis moving platform	13.9 kg
Mass of the PSRM	55.4 kg
Air-gap length	0.3 mm
Range of base plate	600 mm × 600 mm
Phase resistance	0.5 Ω
Number of turns per phase	150

B. Modeling

Since the two sets of three-phase winding of the PSRM are decoupled magnetically, electromagnetic forces of two axes are independently generated with little mutual influence.

The thrust force is represented as [32]

$$f_l(t) = \sum_{k=a}^{c} f_{lk}\left(i_{lk}(t), x_l(t)\right) = \sum_{k=a}^{c} \frac{\partial \int_0^{\tau_{lk}(t)} \varphi_{lk}(t) di_{lk}(t)}{\partial x_l(t)} \tag{1}$$

where x_l and f_l are the position and the thrust force of the l-axis ($l = x, y$), respectively. f_{lk}, i_{lk}, φ_{lk}, and τ_{lk} are the thrust force, the phase current, the flux linkage, and the constant phase current of phase $k(k = a, b, c)$ in the l-axis, respectively.

For a linear magnetic field, the thrust force is derived as [32]

$$f_l(t) = \sum_{k=a}^{c} \frac{1}{2} \frac{dL_{lk}\left(x_l(t)\right)}{dx_l(t)} i_{lk}^2(t) \tag{2}$$

where L_{lk} is the winding inductance of phase k in the l-axis.

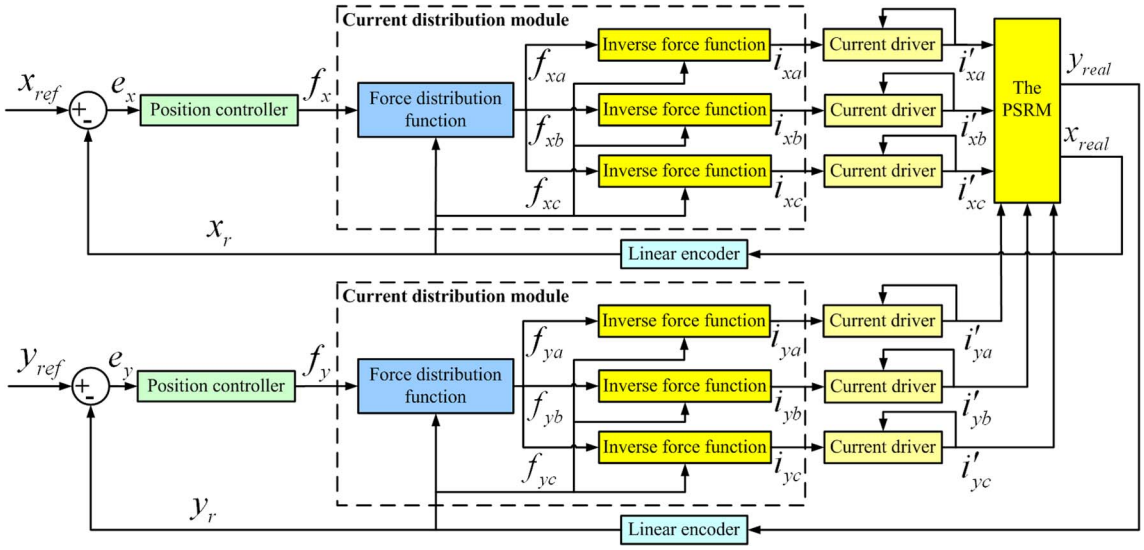

Fig. 2. Block diagram of the PSRM system.

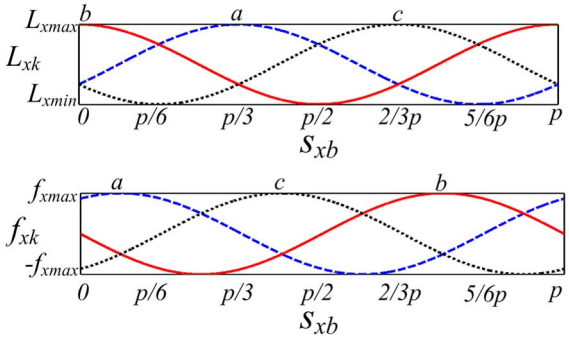

Fig. 3. Inductance profile and generated thrust force of the PSRM in x-axis.

C. Control Strategy

Fig. 2 depicts the block diagram of the PSRM system. For x-axis linear motion, the actual position x_{real} is detected and transformed into the position signal x_r through an x-axis linear encoder. x_r is compared with the reference position x_{ref}, and their position error e_x is processed to produce the thrust force command f_x via an x-axis position controller. In terms of f_x and x_r, the three-phase current commands i_{xa}, i_{xb}, and i_{xc} are obtained from the current distribution. i_{xa}, i_{xb}, i_{xc}, and the detected three-phase current i'_{xa}, i'_{xb}, and i'_{xc} are processed via current drivers to provide three-phase current to the PSRM for achieving x-axis linear motion.

D. Current Distribution

From the x-axis current distribution module shown in Fig. 2, the three-phase thrust force commands f_{xa}, f_{xb}, and f_{xc} are generated via the force distribution function of f_x and x_r. i_{xa}, i_{xb}, and i_{xc} are obtained by inverse force functions according to x_r, f_{xa}, f_{xb}, and f_{xc}.

The operation of the PSRM follows the inductance profile. The inductance profile and generated thrust force of the x-axis under a linear magnetic field are shown in Fig. 3. p is the pole pitch, and $f_{x\max}$, $L_{x\max}$, and $L_{x\min}$ are the maximum thrust force, the maximum inductance, and the minimum inductance of single phase, respectively. $s_{xb} \in [0, p]$ is the overlapped position of phase xb between the stator and mover poles, and the position where the stator and mover poles are completely overlapping for s_{xb} is selected as the origin. Due to the periodic change of the inductance with respect to s_{xb}, f_{xa}, f_{xb}, and f_{xc} can be expressed as

$$\begin{aligned} f_{xa} &= \frac{\pi L_{x\Delta} i_{xa}^2}{p} \sin\left(\frac{2\pi s_{xb}}{p} + \frac{\pi}{3}\right) \\ f_{xb} &= -\frac{\pi L_{x\Delta} i_{xb}^2}{p} \sin\left(\frac{2\pi s_{xb}}{p}\right) \\ f_{xc} &= \frac{\pi L_{x\Delta} i_{xc}^2}{p} \sin\left(\frac{2\pi s_{xb}}{p} - \frac{\pi}{3}\right) \end{aligned} \tag{3}$$

where $L_{x\Delta} = L_{x\max} - L_{x\min}$ [33].

From (3), the x-axis inverse force functions of three-phase winding are represented as

$$\begin{aligned} i_{xa} &= \sqrt{\frac{p f_{xa}}{\pi L_{x\Delta} \sin\left(\frac{2\pi s_{xb}}{p} + \frac{\pi}{3}\right)}} \\ i_{xb} &= \sqrt{\frac{-p f_{xb}}{\pi L_{x\Delta} \sin\left(\frac{2\pi s_{xb}}{p}\right)}} \\ i_{xc} &= \sqrt{\frac{p f_{xc}}{\pi L_{x\Delta} \sin\left(\frac{2\pi s_{xb}}{p} - \frac{\pi}{3}\right)}}. \end{aligned} \tag{4}$$

The force distribution function of the x-axis listed in Table II [34] is exploited, where g_{xa}, g_{xb}, and g_{xc} are given by

$$\begin{aligned} g_{xa} &= \frac{\pi L_{x\Delta}}{p} \sin\left(\frac{2\pi s_{xb}}{p} + \frac{\pi}{3}\right) \\ g_{xb} &= -\frac{\pi L_{x\Delta}}{p} \sin\left(\frac{2\pi s_{xb}}{p}\right) \\ g_{xc} &= \frac{\pi L_{x\Delta}}{p} \sin\left(\frac{2\pi s_{xb}}{p} - \frac{\pi}{3}\right). \end{aligned} \tag{5}$$

TABLE II
FORCE DISTRIBUTION FUNCTION OF x-AXIS

	$f_x \geq 0$	$f_x < 0$
f_{xa}	$f_x \quad s_{xb} \in \left[0 \ \frac{p}{6}\right]$ $\frac{g_{xa}^2}{g_{xa}^2+g_{xc}^2} f_x \quad s_{xb} \in \left(\frac{p}{6} \ \frac{p}{3}\right)$ $\frac{g_{xa}^2}{g_{xa}^2+g_{xb}^2} f_x \quad s_{xb} \in \left(\frac{5p}{6} \ p\right)$ $0 \quad s_{xb} \in \left[\frac{p}{3} \ \frac{5p}{6}\right] \cup p$	$f_x \quad s_{xb} \in \left[\frac{p}{2} \ \frac{2p}{3}\right]$ $\frac{g_{xa}^2}{g_{xa}^2+g_{xc}^2} f_x \quad s_{xb} \in \left(\frac{2p}{3} \ \frac{5p}{6}\right)$ $\frac{g_{xa}^2}{g_{xa}^2+g_{xb}^2} f_x \quad s_{xb} \in \left(\frac{p}{3} \ \frac{p}{2}\right)$ $0 \quad s_{xb} \in \left[0 \ \frac{p}{3}\right] \cup \left[\frac{5p}{6} \ p\right]$
f_{xb}	$f_x \quad s_{xb} \in \left[\frac{2p}{3} \ \frac{5p}{6}\right]$ $\frac{g_{xb}^2}{g_{xb}^2+g_{xc}^2} f_x \quad s_{xb} \in \left(\frac{p}{2} \ \frac{2p}{3}\right)$ $\frac{g_{xb}^2}{g_{xa}^2+g_{xb}^2} f_x \quad s_{xb} \in \left(\frac{5p}{6} \ p\right)$ $0 \quad s_{xb} \in \left[0 \ \frac{p}{2}\right] \cup p$	$f_x \quad s_{xb} \in \left[\frac{p}{6} \ \frac{p}{3}\right]$ $\frac{g_{xb}^2}{g_{xb}^2+g_{xc}^2} f_x \quad s_{xb} \in \left(0 \ \frac{p}{6}\right)$ $\frac{g_{xb}^2}{g_{xa}^2+g_{xb}^2} f_x \quad s_{xb} \in \left(\frac{p}{3} \ \frac{p}{2}\right)$ $0 \quad s_{xb} \in \left[\frac{p}{2} \ p\right] \cup 0$
f_{xc}	$f_x \quad s_{xb} \in \left[\frac{p}{3} \ \frac{p}{2}\right]$ $\frac{g_{xc}^2}{g_{xa}^2+g_{xc}^2} f_x \quad s_{xb} \in \left(\frac{p}{6} \ \frac{p}{3}\right)$ $\frac{g_{xc}^2}{g_{xb}^2+g_{xc}^2} f_x \quad s_{xb} \in \left(\frac{p}{2} \ \frac{2p}{3}\right)$ $0 \quad s_{xb} \in \left[0 \ \frac{p}{6}\right] \cup \left[\frac{2p}{3} \ p\right]$	$f_x \quad s_{xb} \in \left[\frac{5p}{6} \ p\right] \cup 0$ $\frac{g_{xc}^2}{g_{xa}^2+g_{xc}^2} f_x \quad s_{xb} \in \left(\frac{2p}{3} \ \frac{5p}{6}\right)$ $\frac{g_{xc}^2}{g_{xb}^2+g_{xc}^2} f_x \quad s_{xb} \in \left(0 \ \frac{p}{6}\right)$ $0 \quad s_{xb} \in \left[\frac{p}{6} \ \frac{2p}{3}\right]$

III. PROPOSED MFPA STRATEGY OF CURRENT DISTRIBUTION

A. Proposed Current Distribution

The production of electromagnetic forces relies on the inductance change for the SRM. It is the inductance change rate dL_{lk}/dx_l and square of phase current i_{lk}^2 that determine the thrust force of single phase f_{lk} in terms of (2). For the three-phase mover at a fixed position, the phase with a larger dL_{lk}/dx_l produces a larger f_{lk} at a fixed phase current, and it is offered a smaller i_{lk}^2 to generate a constant f_{lk}. Hence, the phase with a larger dL_{lk}/dx_l has larger thrust force per square ampere and smaller copper losses per thrust force. The total thrust force of the l-axis f_l results from the linear superposition of the three-phase thrust force according to (1). Therefore, there are infinitely many combinations of l-axis three-phase current to generate a specific f_l at a fixed position.

The conventional current distribution strategy described in Section II is applied to output low-ripple three-phase current to generate a total thrust force with low ripple. Despite the fact that the excited phases have a big difference in the inductance change rate, they make similar contribution to the total thrust force. Thus, the strategy aiming at lower force ripple suffers from lower efficiency since it does not take full advantage of the phase with a larger inductance change rate. Under this condition, the phase is capable of producing larger thrust force per square ampere and smaller copper losses per thrust force. The MFPA strategy given in this section is employed to optimize the three-phase current to generate a total thrust force with minimum sum of squares of the three-phase current, and it provides larger current to the phase with a larger inductance change rate. The phase with larger thrust force per square ampere and smaller copper losses per thrust force is the main contributor of the total thrust force. Hence, compared with the conventional strategy, the MFPA strategy can generate a specific total thrust force with higher ripple and much smaller sum of squares of the three-phase current for improving efficiency.

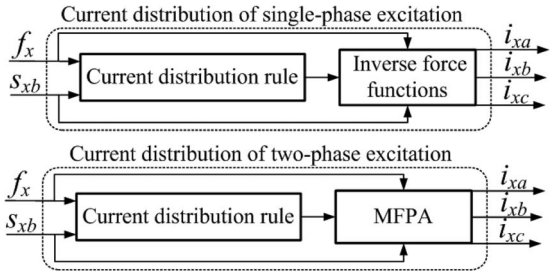

Fig. 4. Current distribution of x-axis based on the MFPA strategy.

TABLE III
CURRENT DISTRIBUTION RULE OF x-AXIS

S_{xb}	$f_x > 0$	$f_x < 0$
0 or p	i_{xa}	i_{xc}
(0 $p/6$)	i_{xa}	i_{xb}, i_{xc}
$p/6$	i_{xa}	i_{xb}
($p/6$ $p/3$)	i_{xa}, i_{xc}	i_{xb}
$p/3$	i_{xc}	i_{xb}
($p/3$ $p/2$)	i_{xc}	i_{xa},i_{xb}
$p/2$	i_{xc}	i_{xa}
($p/2$ $2p/3$)	i_{xb}, i_{xc}	i_{xa}
$2p/3$	i_{xb}	i_{xa}
($2p/3$ $5p/6$)	i_{xb}	i_{xa}, i_{xc}
$5p/6$	i_{xb}	i_{xc}
($5p/6$ p)	i_{xa},i_{xb}	i_{xc}

The current distribution with the MFPA strategy for the PSRM in the x-axis is shown in Fig. 4. f_x and s_{xb} are inputs of the current distribution, and they are mapped into the current distribution rule listed in Table III to determine the excited phases.

For single-phase excitation, a specific i_{lk} is used to generate a specific f_x in terms of (2), and the excited i_{lk} is obtained via inverse force functions given in (4). For two-phase excitation, there are infinitely many combinations of two-phase current to produce specific f_x from (2), and thus, the MFPA is applied to attain optimal two-phase current for efficiency optimization.

Since the maximum number of excited phases is two, the sum of squares of the three-phase current command i_t for two-phase excitation is represented as

$$i_t = i_{xa}^2 + i_{xb}^2 + i_{xc}^2 = i_{xj}^2 + i_{xk}^2, \quad j = a,b,c; \quad k = a,b,c; \quad j \neq k \tag{6}$$

where $i_{xj} \geq 0$, $i_{xk} \geq 0$, and $i_t \geq 0$, as the PSRM is based on the switched reluctance principle.

TABLE IV
COMBINATIONS OF β, η, AND $i_{xj}+i_{xk}$

$i_{xj}+i_{xk}$	β	η
$i_{xa}+i_{xb}$	$\frac{\pi L_{x\Delta}}{p}\sin(\frac{2\pi s_{xb}}{p}+\frac{\pi}{3})$	$-\frac{\pi L_{x\Delta}}{p}\sin(\frac{2\pi s_{xb}}{p})$
$i_{xa}+i_{xc}$	$\frac{\pi L_{x\Delta}}{p}\sin(\frac{2\pi s_{xb}}{p}+\frac{\pi}{3})$	$\frac{\pi L_{x\Delta}}{p}\sin(\frac{2\pi s_{xb}}{p}-\frac{\pi}{3})$
$i_{xb}+i_{xc}$	$-\frac{\pi L_{x\Delta}}{p}\sin(\frac{2\pi s_{xb}}{p})$	$\frac{\pi L_{x\Delta}}{p}\sin(\frac{2\pi s_{xb}}{p}-\frac{\pi}{3})$

B. Proposed MFPA Strategy

For the PSRM generating desired $f_x \neq 0$ by two-phase excitation, the MFPA operating condition is achieved only for solving the constrained optimization problem

$$\begin{aligned} \min \quad & i_t = i_{xj}^2 + i_{xk}^2 = i_{xj}^2 + \frac{f_x - \beta i_{xj}^2}{\eta} \\ \text{s.t.} \quad & i_{xj} \geq 0, \quad \lambda - i_{xj} \geq 0, \quad \left(\frac{f_x - \beta i_{xj}^2}{\eta}\right)^{\frac{1}{2}} \geq 0 \\ & \lambda - \left(\frac{f_x - \beta i_{xj}^2}{\eta}\right)^{\frac{1}{2}} \geq 0 \end{aligned} \tag{7}$$

where $f_x = \beta i_{xj}^2 + \eta i_{xk}^2$, λ is the maximum phase current, $\beta \neq 0$ and $\eta \neq 0$ are time-varying parameters with respect to f_x and s_{xb}, and f_x, β, and η have the same sign. From (2) and (3), the combinations of β, η, and $i_{xj}+i_{xk}$ are listed in Table IV.

To gain the minimum i_t, the AGA is used to solve (7) for locating the optimal i_{xj} and i_{xk}. For better solving (7) by the AGA, the barrier function is utilized to transform (7) into an unconstrained optimization problem as

$$\min \ F(i_{xj}, r) = i_{xj}^2 + \frac{f_x - \beta i_{xj}^2}{\eta} + rH(i_{xj}) \tag{8}$$

where $r > 0$ is a penalty factor; $H(i_{xj})$ is deduced from the constraints of (7), and it is given as

$$\begin{aligned} H(i_{xj}) = i_{xj}^{-1} + (\lambda - i_{xj})^{-1} + \left(\frac{f_x - \beta i_{xj}^2}{\eta}\right)^{-\frac{1}{2}} \\ + \left(\lambda - \left(\frac{f_x - \beta i_{xj}^2}{\eta}\right)^{\frac{1}{2}}\right)^{-1}. \end{aligned} \tag{9}$$

For (8), if i_{xj} is in the constraints of (7), the value of r is sufficiently small such that $F(i_{xj}, r)$ has a small value. If not, the value of r is very large such that $F(i_{xj}, r)$ has a large value.

IV. AGA

An AGA is developed to solve (8) for obtaining the optimal i_{xj}. The flowchart of the AGA is shown in Fig. 5.

The real number encoding is utilized to the chromosome encoding. The chromosome can be directly represented as the individual with this encoding. Hence, $i_{xj} \in [0, \lambda]$ is selected as the chromosome.

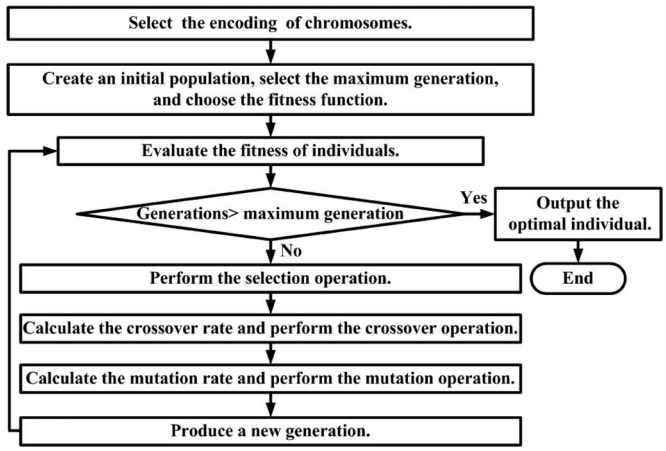

Fig. 5. Flowchart of the AGA.

A. Fitness Function

The fitness function is used to provide a search direction for finding the optimal individual in the selection process. Employing the penalty criterion, the fitness function is chosen, and the evaluation criterion is that the smaller the fitness value is, the better the individual is. The fitness function is represented as

$$w(i_{xj}) = \begin{cases} i_{xj}^2 + \frac{f_x - \beta i_{xj}^2}{\eta} + 0.1\,H(i_{xj}), & i_{xj} \in D \\ 10000, & i_{xj} \notin D \end{cases} \tag{10}$$

where a high fitness value is assigned to the solutions that violates D, and D formulating the constraints of (7) is expressed as

$$\begin{aligned} D = \Bigg\{ & i_{xj} \in \boldsymbol{R} \,|\, \{i_{xj} \geq 0\} \cap \{\lambda - i_{xj} \geq 0\} \\ & \cap \left\{\left(\frac{f_x - \beta i_{xj}^2}{\eta}\right)^{\frac{1}{2}} \geq 0\right\} \cap \left\{\lambda - \left(\frac{f_x - \beta i_{xj}^2}{\eta}\right)^{\frac{1}{2}} \geq 0\right\}\Bigg\}. \end{aligned} \tag{11}$$

B. Selection Operation

The selection operation is to select the individuals with better fitness values. A hybrid strategy of adaptive ranking selection and elitist selection is employed.

The adaptive ranking selection is depicted as follows.

1) The population is sorted by descending fitness values.
2) A probability distribution is designed, and each of the probability values assigned to each individual is sorted by fitness values.
3) With the probability values, the roulette wheel selection [28] is applied to generate the population of the next generation.

The designed probability distribution is given as

$$p_s(n) = \frac{1}{N}\left(\rho^+ - \frac{\rho^+ - \rho-}{N-1}(n-1)\right)$$
$$\rho^+ = 1 + \frac{f_{\text{avg}}}{f_{\max}},\ n = 1, \ldots, N \tag{12}$$

where $\rho^+ + \rho^- = 2$, $1 \le \rho^+ \le 2$, N is the population size, $p_s(n)$ is the probability value of the nth individual, and $f_{\max}$ and f_{avg} are the maximum and average fitness values, respectively.

The elitist selection process is described as follows.

1) The individuals with the highest and smallest fitness values are determined.
2) If the fitness value of the best individual in the current generation is better than that of the previous generation, the best individual of the current generation is retained in the next generation. If not, the worst individual of the current generation, which has performed crossover and mutation operations, is replaced by the best individual of the previous generation.

C. Adaptive Crossover Operation

The crossover operation creates new and improved chromosomes. A nonuniform crossover is utilized and given by

$$\begin{cases} z_1' = \alpha_2 z_1 + (1-\alpha_2) z_2 \\ z_2' = \alpha_2 z_2 + (1-\alpha_2) z_1 \end{cases}, \quad \alpha_1 < p_c \tag{13}$$

where $\alpha_1 \in [0,\ 1]$ and $\alpha_2 \in [0,\ 1]$ are random numbers, z_1 and z_2 are the individuals of the current generation, z_1' and z_2' are the created individuals of the next generation, and the adaptive crossover operator p_c is represented as

$$p_c = \begin{cases} p_{c1} - \frac{(p_{c1}-p_{c2})(f'-f_{\text{avg}})}{f_{\max}-f_{\text{avg}}}, & f' \ge f_{\text{avg}} \\ p_{c1}, & f' < f_{\text{avg}} \end{cases} \tag{14}$$

where f' is the better fitness value between z_1 and z_2, $p_{c1} = 0.9$, and $p_{c2} = 0.6$.

D. Adaptive Mutation Operation

The mutation operation is to preserve and introduce diversity. The mutation operation is selected as

$$y_1' = \begin{cases} y_1 + \alpha_4(0 - y_1), & \alpha_3 < p_m \text{ and } \alpha_4 \ge 0.5 \\ y_1 + \alpha_4(\lambda - y_1), & \alpha_3 < p_m \text{ and } \alpha_4 < 0.5 \end{cases} \tag{15}$$

where $\alpha_3 \in [0,\ 1]$ and $\alpha_4 \in [0,\ 1]$ are random numbers, y_1 is the individual of the current generation, y'_1 is the created individual of the next generation, and the adaptive mutation operator p_m is

$$p_m = \begin{cases} p_{m1} - \frac{(p_{m1}-p_{m2})(f_{\max}-f)}{f_{\max}-f_{\text{avg}}}, & f \ge f_{\text{avg}} \\ p_{m1}, & f < f_{\text{avg}} \end{cases} \tag{16}$$

where f is the fitness value of y_1, $p_{m1} = 0.1$, and $p_{m2} = 0.001$.

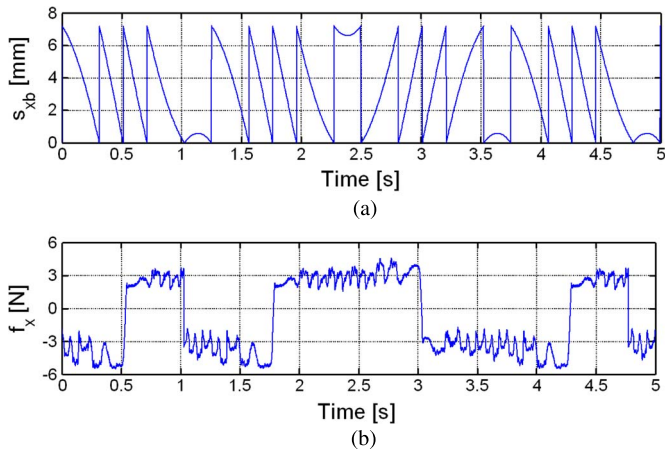

Fig. 6. (a) Overlapped position of phase xb s_{xb}. (b) Thrust force command f_x.

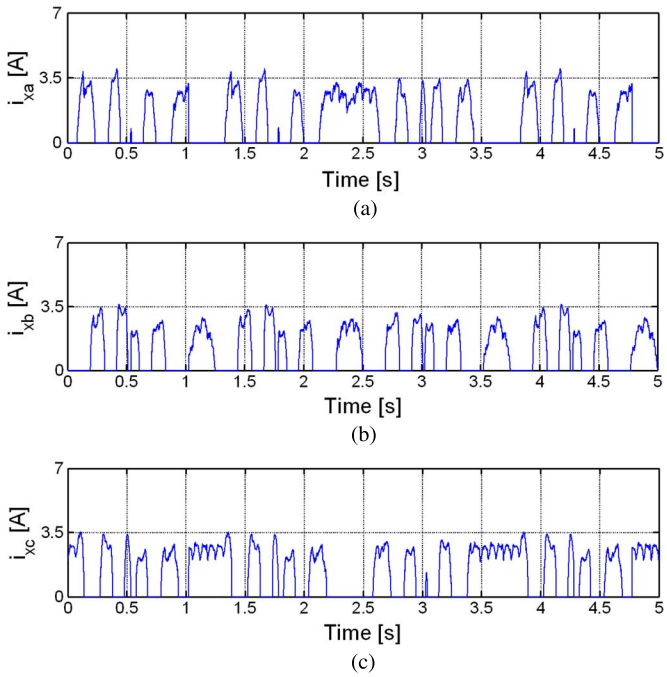

Fig. 7. Three-phase current command of the conventional strategy. (a) i_{xa}. (b) i_{xb}. (c) i_{xc}.

V. Simulation Results

To verify the validity of the proposed current distribution strategy of the PSRM, for an x-axis linear motion, a comparative study of the proposed and conventional current distribution strategies is carried out under the same condition, based on MATLAB/Simulink.

The inputs of both simulation systems are the x-axis thrust force command f_x and overlapped position of phase xb s_{xb}. f_x is from the x-axis position controller, and s_{xb} is from the x-axis linear encoder. To simulate a real-life practical system, f_x and s_{xb} are obtained from experimental measurement, and they are presented in Fig. 6. The maximum current command is 10 A. The population size and the maximum generation of the AGA are selected as 30 and 200, respectively.

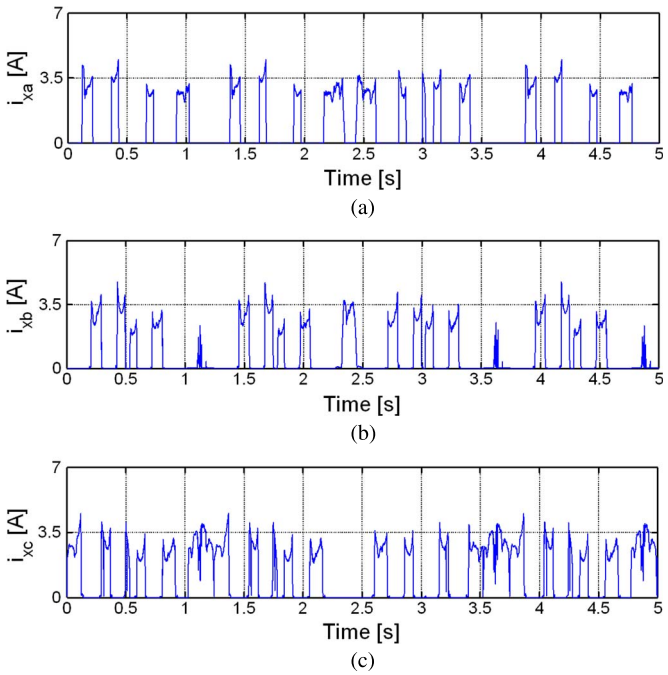

Fig. 8. Three-phase current command of the proposed strategy. (a) i_{xa}. (b) i_{xb}. (c) i_{xc}.

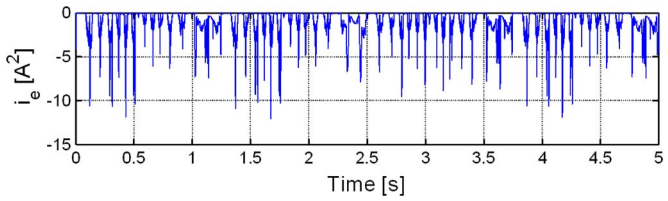

Fig. 9. Difference i_e.

The three-phase current commands i_{xa}, i_{xb}, and i_{xc} from the conventional and proposed strategies are shown in Figs. 7 and 8, respectively. The shapes of the waveforms of i_{xa}, i_{xb}, and i_{xc} from the proposed strategy are substantially consistent with those from the conventional strategy. In the time from 2.278 to 2.494 s, the excited phases of the two strategies are phases xa and xb, and the magnitudes of i_{xa} and i_{xb} from the conventional strategy have no significant difference. For the proposed strategy in the same instant range, i_{xa} and i_{xb} are almost zero for a short period of time since phases xa and xb have a much smaller inductance change rate with less contribution to the total thrust force at that time. The magnitudes of i_{xa} and i_{xb} have no significant difference for the remaining time, as phases xa and xb have similar inductance change rate with similar contribution to the total thrust force at that time. Fig. 9 depicts the difference i_e. i_e denotes the sum of squares of the three-phase current command i_t from the proposed strategy minus that from the conventional strategy. Each value of i_t from the conventional strategy is higher than that from the proposed strategy. The mean values of i_t of the two strategies are listed in Table V. The mean value of i_t of the proposed strategy is reduced by 10.78% compared with that of the conventional strategy.

TABLE V
SUM OF SQUARES OF THE THREE-PHASE CURRENT

	Mean value of i_t for simulation	Mean value of i_t for experiment	Mean value of i_t' for experiment
Conventional current distribution strategy	9.2578 A^2	9.4223 A^2	9.8170 A^2
Proposed current distribution strategy	8.2596 A^2	8.3604 A^2	8.6655 A^2

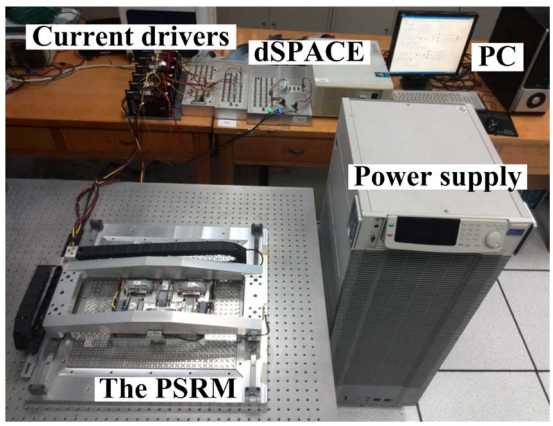

Fig. 10. Experimental setup of the PSRM system.

In comparison with the conventional strategy, the proposed strategy is capable of producing the desired thrust force with much smaller sum of squares of the three-phase current, and its efficiency is increased with the copper losses decreased by 10.78%. Thus, the proposed strategy can improve the efficiency of the PSRM substantially.

VI. EXPERIMENTAL VERIFICATION

A. Experimental Setup

Fig. 10 shows the experimental setup of the PSRM system. Two linear optical encoders from Renishaw's Tonic series with dual resolutions of 100 and 50 nm are used to detect the positions of both axes. Six 50A20 servo drives of advanced motion controls are applied as direct current (dc) current drivers to offer currents to the excited phase windings. The control algorithm is designed based on MATLAB/Simulink, and it is downloaded to dSPACE modular hardware for realizing real-time control. The utilized dSPACE modular hardware includes a DS1005 PPC board, a DS2103 D/A board, and a DS3001 incremental encoder interface board.

B. Experimental Results

To clearly demonstrate the validity of the proposed current distribution strategy of the PSRM, a comparative study of the proposed and conventional current distribution strategies is performed. The inputs of the PSRM system are identical to those of the simulation system manifested in Fig. 6. To improve real-time performance, the proposed current distribution strategy is implemented by a lookup table. The maximum

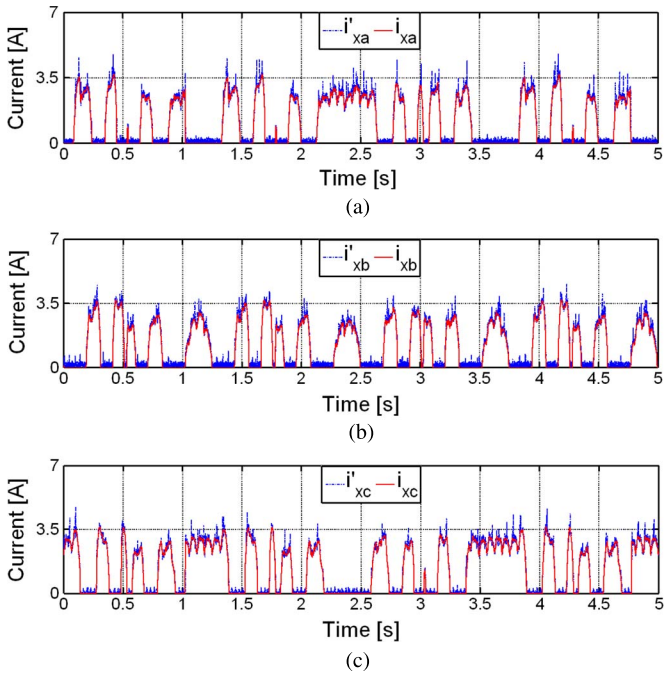

Fig. 11. Three-phase current command and detected three-phase current of the conventional strategy. (a) Phase xa. (b) Phase xb. (c) Phase xc.

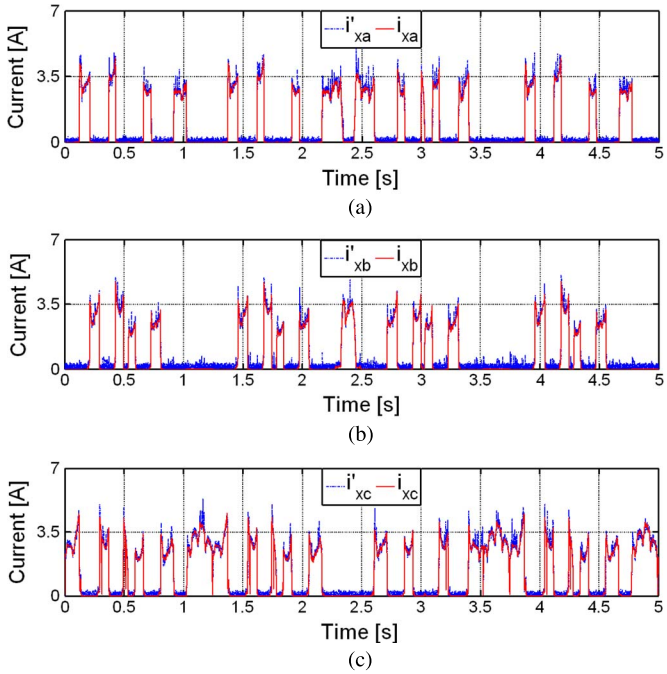

Fig. 12. Three-phase current command and detected three-phase current of the proposed strategy. (a) Phase xa. (b) Phase xb. (c) Phase xc.

current command is 10 A, and the sampling time of the control algorithm is 0.0005 s.

The three-phase current commands i_{xa}, i_{xb}, and i_{xc} and the detected three-phase currents i'_{xa}, i'_{xb}, and i'_{xc} from the conventional and proposed strategies are depicted in Figs. 11 and 12, respectively. The shapes of the waveforms of i_{xa}, i_{xb}, i_{xc}, i'_{xa}, i'_{xb}, and i'_{xc} from the conventional strategy substantially

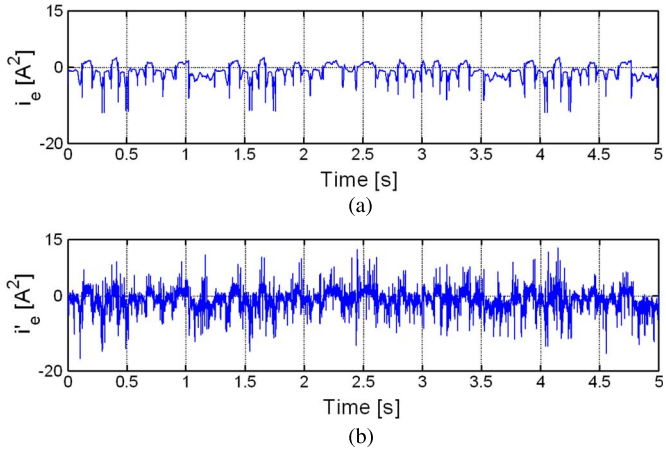

Fig. 13. (a) Difference i_e. (b) Difference i'_e.

coincide with those from the proposed strategy. The shapes of the waveforms in Figs. 11 and 12 are consistent with those in Figs. 7 and 8, respectively. The currents from current drivers quickly track the current commands from the two strategies. The satisfactory real-time performance is consequently achieved. The differences i_e and i'_e are indicated in Fig. 13. i'_e is expressed as the sum of squares of the detected three-phase current i'_t from the proposed strategy minus that from the conventional strategy. Fig. 13 reveals that the magnitudes of i_t and i'_t of the conventional strategy are substantially higher than those of the proposed strategy. Table V lists the mean values of i_t and i'_t of the two strategies. Compared to the conventional strategy, the mean values of i_t and i'_t of the proposed strategy are decreased by 11.27% and 11.73%, respectively. The proposed strategy is capable of producing the desired thrust force with much smaller sum of squares of the three-phase current; the efficiency is increased due to the copper losses reduced by 11.73%.

To further illustrate the feasibility of the proposed strategy, a pentangular trajectory tracking is applied to the PSRM system. A waveform with a maximum amplitude of 30 mm and a frequency of 1/3 Hz is used as the x-axis reference position, while a waveform with a maximum amplitude of 28.53 mm and a frequency of 1/3 Hz is utilized as the y-axis reference position. Two proportional-derivative (PD) controllers are provided to control the x- and y-axis positions. The parameters of the PD controller in x- and y-axes are $k_{px} = 303.5$ and $k_{dx} = 1.1$ and $k_{py} = 561.6$ and $k_{dy} = 1.7$, respectively. The bandwidths of the closed-loop position control for x- and y-axes are 61.9 and 52.5 Hz, respectively. The maximum current command is 10 A, the thrust force command is limited to 30 N, and the sampling time of the control algorithm is 0.0005 s.

Fig. 14 shows the current commands and detected currents of the PSRM system, and it manifests that the currents from current drivers quickly track the current commands from the proposed current distribution. The thrust force commands of two axes from PD controllers are presented in Fig. 15. Fig. 16 depicts the planar trajectory tracking response, the position responses of two axes, and the speed responses of two axes. In Fig. 16(c), vx_{ref}, vx_r, vy_{ref}, and vy_r are the x-axis reference speed, x-axis detected speed, y-axis reference speed,

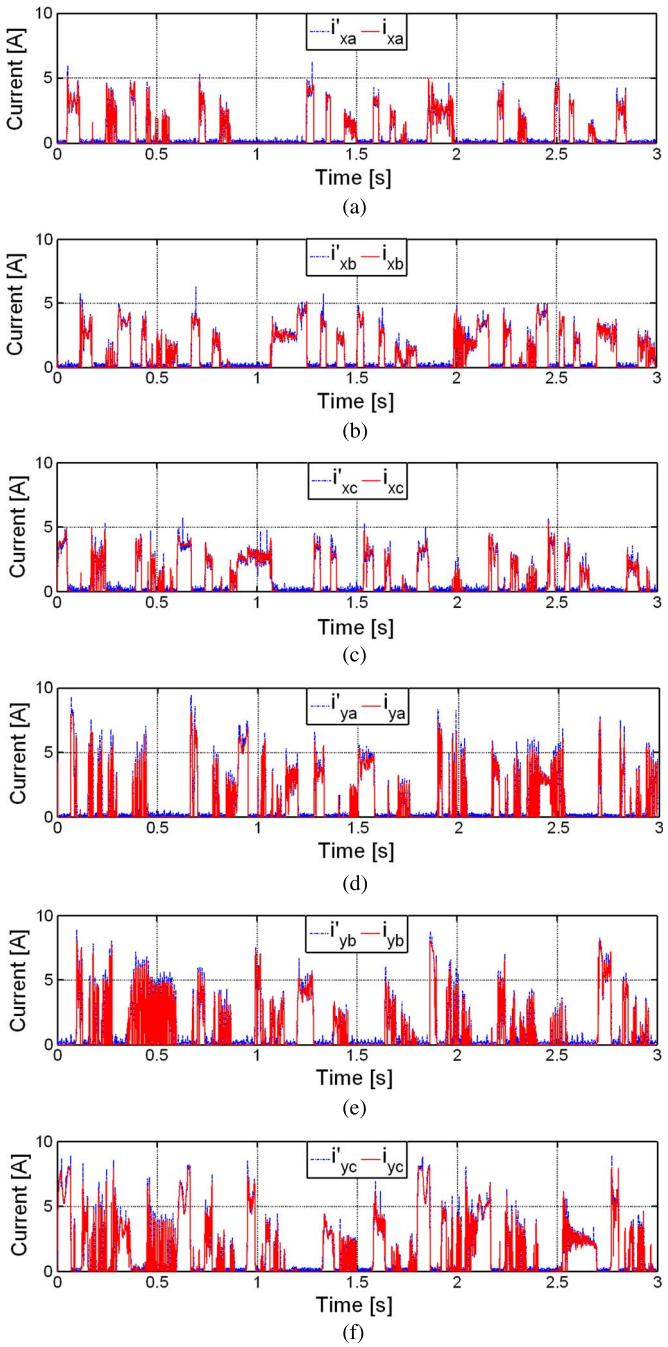

Fig. 14. Current commands and detected currents. (a) Phase xa. (b) Phase xb. (c) Phase xc. (d) Phase ya. (e) Phase yb. (f) Phase yc.

and y-axis detected speed, respectively. The position errors of two axes are indicated in Fig. 17(a). Figs. 16 and 17(a) reveal that the system exhibits satisfactory dynamic and steady-state performances since it tracks the given pentangular trajectory smoothly, quickly, and precisely. To further validate the effectiveness of the proposed strategy, the position errors of the PSRM system with the conventional strategy under the same condition are acquired and manifested in Fig. 17(b). It can be noticed that the general trend of the position errors for the two strategies is consistent within one cycle of the trajectory tracking because the thrust force commands of the two strategies are similar under the same operating condition.

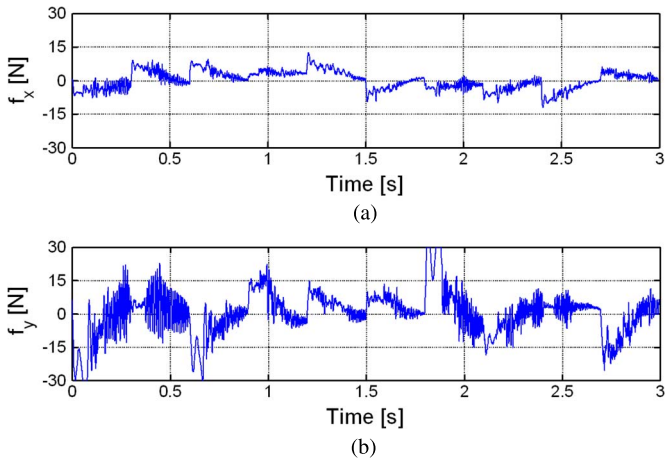

Fig. 15. Thrust force commands. (a) x-axis. (b) y-axis.

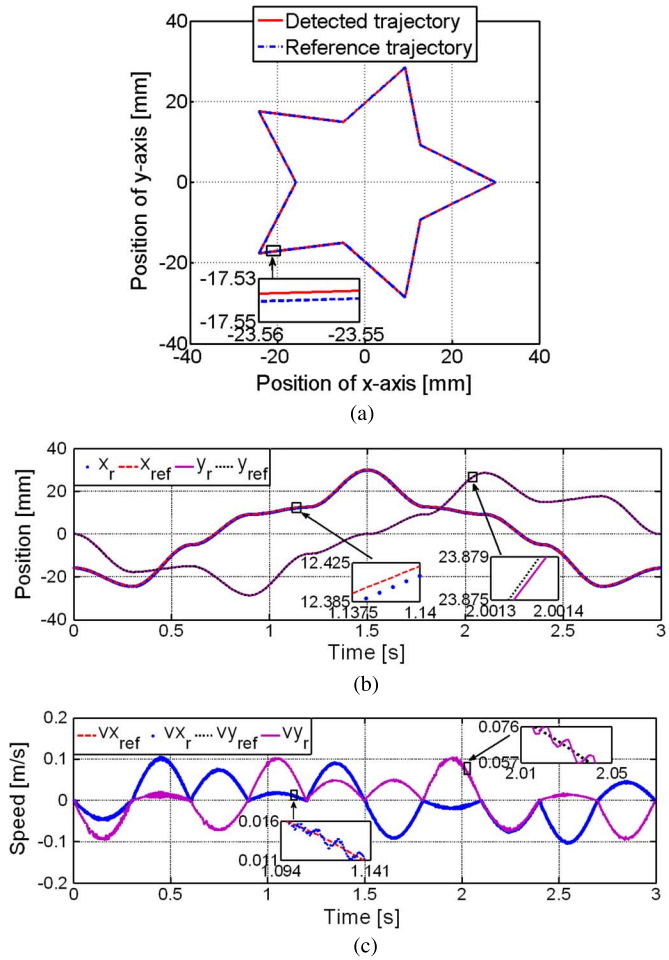

Fig. 16. (a) Planar trajectory tracking response of the PSRM system. (b) Position responses of x- and y-axes. (c) Speed responses of x- and y-axes.

The absolute position errors of the trajectory tracking for the proposed and conventional strategies are less than 91.2 and 56.1 μm, respectively. For the proposed strategy, the position errors increase versus the conventional strategy since the less smooth optimal three-phase current results in the slightly larger vibration. It is found that there is a tradeoff between the efficiency and the positioning accuracy for the current distribution.

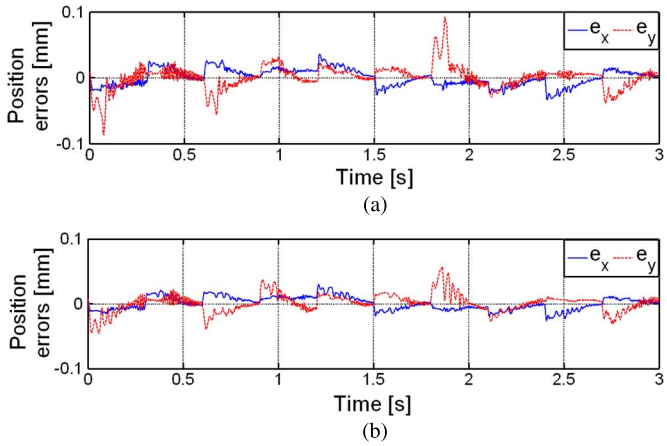

Fig. 17. Position errors. (a) Proposed strategy. (b) Conventional strategy.

Although the position errors increase, the proposed strategy is aimed at improving the efficiency in the presence of satisfactory dynamic and steady-state performances.

The aforementioned analysis proves that the proposed strategy is valid, and it can be readily implemented for any real-time control application.

VII. Conclusion

In this paper, a novel MFPA strategy of the current distribution for the PSRM has been proposed to improve the efficiency. An AGA has been implemented to solve the unconstrained optimization problem of the MFPA. From the simulation and experimental results, some conclusions can be drawn: 1) Compared to the conventional strategy, the proposed strategy is capable of generating the desired thrust force with higher ripple and much smaller three-phase current, resulting in an increase of the efficiency; 2) the PSRM system with the proposed strategy exhibits increased vibration and satisfactory dynamic and steady-state performances; and 3) the proposed strategy is a better alternative to the current distribution strategy for efficiency improvement of the PSRM. The proposed strategy can also be applied to other similar types of motors, such as the rotary SRM and the LSRM.

References

[1] Q. Xu, "Design and development of a compact flexure-based XY precision positioning system with centimeter range," *IEEE Trans. Ind. Electron.*, vol. 61, no. 2, pp. 893–903, Feb. 2014.

[2] J. L. Perez-Diaz, I. Valiente-Blanco, E. Diez-Jimenez, and J. Sanchez-Garcia-Casarrubios, "Superconducting noncontact device for precision positioning in cryogenic environments," *IEEE/ASME Trans. Mechatronics*, vol. 19, no. 2, pp. 598–605, Apr. 2014.

[3] U. Bhagat *et al.*, "Experimental investigation of robust motion tracking control for a 2-DOF flexure-based mechanism," *IEEE/ASME Trans. Mechatronics*, vol. 19, no. 6, pp. 1737–1745, Dec. 2014.

[4] M.-Y. Chen, H.-H. Huang, and S.-K. Hung, "A new design of a submicropositioner utilizing electromagnetic actuators and flexure mechanism," *IEEE Trans. Ind. Electron.*, vol. 57, no. 1, pp. 96–106, Jan. 2010.

[5] J. M. M. Rovers, J. W. Jansen, J. C. Compter, and E. A. Lomonova, "Analysis method of the dynamic force and torque distribution in the magnet array of a commutated magnetically levitated planar actuator," *IEEE Trans. Ind. Electron.*, vol. 59, no. 5, pp. 2157–2166, May 2012.

[6] L. Zhang, B. Kou, L. Li, and B. Zhao, "Modeling and design of an integrated winding synchronous permanent magnet planar motor," *IEEE Trans. Plasma Sci.*, vol. 41, no. 5, pp. 1214–1219, May 2013.

[7] J. W. Jansen, J. P. C. Smeets, T. T. Overboom, J. M. M. Rovers, and E. A. Lomonova, "Overview of analytical models for the design of linear and planar motors," *IEEE Trans. Magn.*, vol. 50, no. 11, Nov. 2014, Art. ID 8206207.

[8] J. Pan, N. C. Cheung, and J. Yang, "High-precision position control of a novel planar switched reluctance motor," *IEEE Trans. Ind. Electron.*, vol. 52, no. 6, pp. 1644–1652, Dec. 2005.

[9] H. Hayashi *et al.*, "Efficiency improvements of switched reluctance motors with high-quality iron steel and enhanced conductor slot fill," *IEEE Trans. Energy Convers.*, vol. 24, no. 4, pp. 819–825, Dec. 2009.

[10] A. E. K. Mohammad, N. Uchiyama, and S. Sano, "Reduction of electrical energy consumed by feed-drive systems using sliding-mode control with a nonlinear sliding surface," *IEEE Trans. Ind. Electron.*, vol. 61, no. 6, pp. 2875–2882, Jun. 2014.

[11] K.-W. Lee, S. Park, and S. Jeong, "A seamless transition control of sensorless PMSM compressor drives for improving efficiency based on a dual-mode operation," *IEEE Trans. Power Electron.*, vol. 30, no. 3, pp. 1446–1456, Mar. 2015.

[12] S.-Y. Jung, C. C. Mi, and K. Nam, "Torque control of IPMSM in the field-weakening region with improved dc-link voltage utilization," *IEEE Trans. Ind. Electron.*, vol. 62, no. 6, pp. 3380–3387, Jun. 2015.

[13] A. Consoli, G. Scelba, G. Scarcella, and M. Cacciato, "An effective energy-saving scalar control for industrial IPMSM drives," *IEEE Trans. Ind. Electron.*, vol. 60, no. 9, pp. 3658–3669, Sep. 2013.

[14] M. Dems and K. Komeza, "Performance characteristics of a high-speed energy-saving induction motor with an amorphous stator core," *IEEE Trans. Ind. Electron.*, vol. 61, no. 6, pp. 3046–3055, Jun. 2014.

[15] H.-S. Cho, C.-H. Im, and H.-K. Jung, "Magnetic field analysis of 2-D permanent magnet array for planar motor," *IEEE Trans. Magn.*, vol. 37, no. 5, pp. 3762–3766, Sep. 2001.

[16] W. Min *et al.*, "Analysis and design of novel overlapping ironless windings for planar motors," *IEEE Trans. Magn.*, vol. 47, no. 11, pp. 4635–4642, Nov. 2011.

[17] G. Zhou, X. Huang, H. Jiang, and Z. Wang, "A novel ohmic-loss reduction control strategy for planar motor," *IEEE Trans. Magn.*, vol. 48, no. 11, pp. 2997–3000, Nov. 2012.

[18] C. M. M. van Lierop, J. W. Jansen, A. A. H. Damen, and P. P. J. van den Bosch, "Control of multi-degree-of-freedom planar actuators," in *Proc. IEEE Int. Conf. Control Appl.*, 2006, pp. 2516–2521.

[19] J. M. M. Rovers, J. W. Jansen, and E. A. Lomonova, "Multiphysical analysis of moving-magnet planar motor topologies," *IEEE Trans. Magn.*, vol. 49, no. 12, pp. 5730–5741, Dec. 2013.

[20] F.-J. Lin, Y.-C. Hung, J.-M. Chen, and C.-M. Yeh, "Sensorless IPMSM drive system using saliency back-EMF-based intelligent torque observer with MTPA control," *IEEE Trans. Ind. Informat.*, vol. 10, no. 2, pp. 1226–1241, May 2014.

[21] T. Sun, J. Wang, and X. Chen, "Maximum torque per ampere (MTPA) control for interior permanent magnet synchronous machine drives based on virtual signal injection," *IEEE Trans. Power Electron.*, vol. 30, no. 9, pp. 5036–5045, Sep. 2015.

[22] R. Antonello, M. Carraro, and M. Zigliotto, "Maximum-torque-per-ampere operation of anisotropic synchronous permanent-magnet motors based on extremum seeking control," *IEEE Trans. Ind. Electron.*, vol. 61, no. 9, pp. 5086–5093, Sep. 2014.

[23] M. Preindl and S. Bolognani, "Optimal state reference computation with constrained MTPA criterion for PM motor drives," *IEEE Trans. Power Electron.*, vol. 30, no. 8, pp. 4524–4535, Aug. 2015.

[24] N. Nakao and K. Akatsu, "Vector control specialized for switched reluctance motor drives," in *Proc. Int. Conf. Elect. Mach.*, 2014, pp. 943–949.

[25] W. Wang and B. Fahimi, "Maximum torque per ampere control of switched reluctance motors," in *Proc. IEEE Energy Convers. Congr. Expo.*, 2012, pp. 4307–4313.

[26] L. Griffin, F. Fleming, and C. S. Edrington, "A particle swarm optimization based maximum torque per ampere control for a switched reluctance motor," in *Proc. 40th Annu. IEEE IECON*, 2014, pp. 343–348.

[27] J. J. Grefenstette, "Optimization of control parameters for genetic algorithms," *IEEE Trans. Syst., Man, Cybern.*, vol. 16, no. 1, pp. 122–128, Jan. 1986.

[28] M. Srinivas and L. M. Patnaik, "Adaptive probabilities of crossover and mutation in genetic algorithms," *IEEE Trans. Syst., Man, Cybern.*, vol. 24, no. 4, pp. 656–667, Apr. 1994.

[29] F. Wang *et al.*, "An improved adaptive genetic algorithm for image segmentation and vision alignment used in microelectronic bonding," *IEEE/ASME Trans. Mechatronics*, vol. 19, no. 3, pp. 916–923, Jun. 2014.

[30] Y. Du, J. Fang, and C. Miao, "Frequency-domain system identification of an unmanned helicopter based on an adaptive genetic algorithm," *IEEE Trans. Ind. Electron.*, vol. 61, no. 2, pp. 870–881, Feb. 2014.

[31] X.-K. Wei, W. Shao, C. Zhang, J.-L. Li, and B.-Z. Wang, "Improved self-adaptive genetic algorithm with quantum scheme for electromagnetic optimisation," *IET Microw. Antennas Propag.*, vol. 8, no. 12, pp. 965–972, Sep. 2014.
[32] R. Krishnan, *Switch Reluctance Motor Derives: Modeling, Simulation, Analysis, Design, and Application*. Boca Raton, FL, USA: CRC Press, 2001.
[33] I. Boldea and S. A. Nasar, *Linear Electric Actuators and Generators*. Cambridge, U.K.: Cambridge Univ. Press, 1997.
[34] H.-K. Bae, B.-S. Lee, P. Vijayraghavan, and R. Krishnan, "A linear switched reluctance motor: Converter and control," *IEEE Trans. Ind. Appl.*, vol. 36, no. 5, pp. 1351–1359, Sep./Oct. 2000.

Su-Dan Huang received the B.Sc. and M.Sc. degrees in control theory and control engineering from Shenzhen University, Shenzhen, China, in 2009 and 2012, respectively. She is currently pursuing a joint Ph.D. degree in electrical engineering at Southwest Jiaotong University, Chengdu, China, and the Shenzhen Key Laboratory of Electromagnetic Control, Shenzhen University.

Her research interests include the design and control of planar switched reluctance motors, and control theory and its applications.

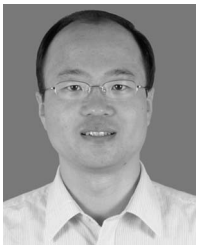

Guang-Zhong Cao (M'15) received the B.Sc., M.Sc., and Ph.D. degrees in electrical engineering and automation from Xi'an Jiaotong University, Xi'an, China, in 1989, 1992, and 1996, respectively.

He is currently a Professor and Director of the Shenzhen Key Laboratory of Electromagnetic Control, Shenzhen University, Shenzhen, China. He has authored more than 80 articles published in refereed journals and conference proceedings. His research interests include motor control, and control theory and its applications.

Zheng-You He (SM'13) received the B.Sc. and M.Sc. degrees in computational mechanics from Chongqing University, Chongqing, China, in 1992 and 1995, respectively, and the Ph.D. degree in electrical engineering from Southwest Jiaotong University, Chengdu, China, in 2001.

He is currently a Professor with the Department of Electrical Engineering, Southwest Jiaotong University. His research interests include signal processing and information theory applied to power systems and applications of wavelet transforms in power systems.

Chao Wu received the B.Sc. and M.Sc. degrees from Southwest Jiaotong University, Chengdu, China, in 2003 and 2006, respectively, and the Ph.D. degree in electrical engineering from Tsinghua University, Beijing, China, in 2010.

She is currently an Associate Professor with the Shenzhen Key Laboratory of Electromagnetic Control, Shenzhen University, Shenzhen, China. Her research interests include power system dynamic analysis and control, and signal processing.

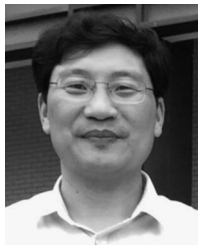

Ji-An Duan received the Ph.D. degree in mechanical engineering from Xi'an Jiaotong University, Xi'an, China, in 1996.

He is currently a Professor and Director of the State Key Laboratory of High-Performance Complex Manufacturing, Central South University, Changsha, China. He has authored more than 60 articles published in refereed journals and conference proceedings. His research interests include advanced manufacturing technology and equipment, and dynamic analysis and control of electromechanical systems.

Norbert C. Cheung (SM'05) received the B.Sc. degree from the University of London, London, U.K., in 1981, the M.Sc. degree from the University of Hong Kong, Kowloon, Hong Kong, in 1987, and the Ph.D. degree from the University of New South Wales, Sydney, Australia, in 1995.

He is currently an Associate Professor with the Department of Electrical Engineering, Hong Kong Polytechnic University, Kowloon, Hong Kong. His research interests include motion control, actuator design, and power electronic drives.

Qing-Quan Qian received the B.Sc. degree in electrical engineering from Southwest Jiaotong University, Chengdu, China, in 1960.

Since 1997, he has been an Academician with the Chinese Academy of Engineering. He is currently a Professor with the Department of Electrical Engineering, Southwest Jiaotong University. His research interests include electrification and automation of rail transit.